Title: A Custom, High-Channel-Count Data Acquisition System for Chemical Species Tomography of Aero-Jet Engine Exhaust Plumes

Authors: E. Fisher, *Member, IEEE*, S-A Tsekenis, Y. Yang, *Member, IEEE*, A. Chighine, *Member, IEEE*, C. Liu, *Member, IEEE*, N. Polydorides, *Member, IEEE*, P. Wright *Member, IEEE,* J. Kliment *Member, IEEE,* K. Ozanyan, *Senior Member, IEEE*, T. Benoy, G. Humphries, D. Wilson, *Member, IEEE*, M. Lengden, *Member, IEEE*, W. Johnstone, *Member, IEEE* and H. McCann.

Abstract: The FLITES project (Fiber-Laser Imaging of gas Turbine Exhaust Species) aims to provide a video-rate imaging (100 fps) diagnostic tool for application to the exhaust plumes of the largest civil aero-jet engines. This remit, enabled by chemical species tomography (CST) currently targeting Carbon Dioxide (CO_2), requires system design that facilitates expansion of multiple parameters. Scalability is needed in order to increase imaging speeds and spatial resolutions and extend the system towards other pertinent gases such as the oxides of Nitrogen and Sulphur and unburnt hydrocarbons. This paper presents a fully-scalable, non-invasive instrument for installation in a commercial engine testing facility, technical challenges having been tackled iteratively through bespoke optical and mechanical design, and it specifically presents the high-speed data acquisition system (DAQ) required. Measurement of gas species concentration is implemented by tunable diode laser absorption with wavelength modulation spectroscopy (TDLAS-WMS) using a custom, high-speed 10-40 MS/s/channel 14-bit DAQ. For CO_2 tomography, the system uses 6 angular projections of 21 beams each. However, the presented DAQ has capacity for 192 fully-parallel 10-Hz to 3-MHz differential inputs, achieving a best-case SNR of 56.5 dB prior to filtering. Twelve Ethernet-connected digitization nodes based on field-programmable gate array (FPGA) technology with software control, are distributed around a 7-m diameter mounting "ring". Hence, the high data rates of 8.96-Gb/s per printed circuit board (PCB) and 107.52 Gb/s for the whole system, can be reduced using local digital lock-in amplifiers (DLIAs). We believe this DAQ system is unique in both the TDLAS and CST literature.

Keywords: Aero-Engine Emissions, Chemical Species Tomography, Tunable Diode Laser Absorption Spectroscopy, Data Acquisition Systems, Aerospace and Aviation.

Manuscript Details: Manuscript received 09 Aug 2018, revised 01 Nov 2018, accepted 04 Jan 2019. This work is funded by the Engineering and Physical Sciences Research Council under grants #EP/J002151/2 and EP/J002178/1. E. Fisher, formerly The University of Edinburgh, is now with Coda-Octopus Products Ltd, Edinburgh, UK. S-A. Tsekenis, Y. Yang, C. Liu, N. Polydorides and H. McCann are with the School of Engineering, University of Edinburgh, UK (e-mail: y.yang@ed.ac.uk). A. Chighine, formerly The University of Edinburgh, is now with Rolls-Royce, Birmingham, UK. P. Wright, J. Kliment and K. Ozanyan are with the School of Electrical and Electronic Engineering, The University of Manchester, UK. T. Benoy, formerly The University of Glasgow, is now with Stiftelsen for Industriell og Teknisk Forskning (SINTEF), Norway. G. Humphries, D. Wilson, M. Lengden and W. Johnstone are with the Department of Electronic and Electrical Engineering, The University of Strathclyde, UK.

I. INTRODUCTION:

The FLITES project seeks to image pollutants in the exhaust plumes of high-bypass aero-jet engines using chemical species tomography (CST). By providing windows on combustion processes, this imaging capability enables i) development of high-efficiency engines, ii) bio-fuel mixture development and iii) reduction in pollutants such as Carbon Dioxide (CO_2), the oxides of Nitrogen and Sulphur (NO_x and SO_x) and small-chain unburnt hydrocarbons. In turn, these goals are mandated by stringent emissions legislation [1]. CST using non-intrusive near-infrared (NIR) measurement can target multiple parameters, such as concentration, pressure and temperature of exhaust plume gas species. Elements of the technique have been deployed successfully for a) CST in automotive engines, b) TDLAS in commercial jet-engines using single-beams [2, 3] and c) small development jet engines using both CST [4] and hyper-spectral imaging cameras [5]. Compared with previous methods [6], this project aims to increase the tomographic imaging rate towards 100 frames/s and achieve spatial resolutions of 10×10 cm throughout the 1.4-1.7 m diameter cross-section of the plume [7, 8]. By obtaining video-rate images and showing scalability towards >200 fps, the dynamics of gas mixing within the plume [5] can start to be observed and will complement existing, intrusive testing. While optical and mechanical challenges have been addressed [7, 8] and issues surrounding tomographic reconstruction with a small number of beams and angular views have been targeted algorithmically [9, 10], the increase in size and complexity of this setup has presented issues for electrical designs [7, 8] and data acquisition [11]. Some of these have been covered in a 2018 I2MTC prelude to this paper [12]. The system is hosted at an aero-engine testing facility operated by Instituto Nacional de Técnica Aerospacial (INTA).

While the specifics of the mechanical setup are discussed elsewhere [7, 8, 10, 11], the harsh environment raises numerous data acquisition challenges. The specifics are covered below using a top-down discussion of system requirements, however high-throughput, hard real-time, fully-synchronized DAQs are well researched with many solutions now becoming standard in tomographic systems [13, 14, 15, 16, 17], many of which use field-programmable gate arrays (FPGAs). For the near-IR CST modality, the noise characteristics of photodiode preamplification have been investigated [18], specifically to optimize the gain, bandwidth and noise performance. Likewise, data acquisition has been achieved using modular, parallel channels with in-situ FPGA-based lock-in amplification specifically for low-cost and high signal-to-noise ratios (SNRs) [13]. This latter technique is employed elsewhere [19, 20, 21, 22], where the common theme is measurement of a modulated carrier giving the near-total rejection of out-of-band noise. The disadvantage however, is often the signal-processing, where a high purity homodyne reference is required alongside analog or digital multiplication. Taking the FPGA-based methods further, Xu [23] extended the DLIA principle towards real-time computation of the first and second harmonic peaks and the normalization of the signal to assess the temperature of a gas. Methods of data management including first-in-first-out (FIFO) memories and direct memory access (DMA) are highlighted in [14], while the concepts of i) hierarchical processing and ii) modular DAQs are exemplified by Hegyesi [15] and Hjertaker [16]. Both show the merits and system design of carrying out digitization as close as possible to the analog detector, and the use of digital nodes with data buffering, FPGA-hardware signal processing and software control capabilities. For Ethernet transfer, which is the only viable, high-speed, long-distance transmission medium suitable, Humbert [17] re-implemented the transmission control protocol / internet protocol (TCP/IP) with hierarchical embedded FPGA-based microprocessors while utilizing hardware blocks to offload tasks from the CPU. While TCP/IP guarantees packet arrival and ordering, the user datagram protocol (UDP) is of lower network

overhead but may require a data interleaving strategy to alleviate packet-loss issues [11]. Towards the back-end of a DAQ, it was found that pre-allocating ping-pong data buffers suitable for DMA within real-time operating systems (RTOS) [24], guaranteed input data-handling interrupt behavior.

This paper discusses enabling technologies and the measured performance of a DAQ designed specifically for the imaging requirements and the industrial environment into which this diagnostic tool is to be used. We note, that despite availability of commercial DAQ systems, the cost becomes prohibitive if those systems are to meet the complex requirements for this instrument. This assessment uses the likely cost if basing the DAQ upon the National Instruments FlexRIO and systems available from both Amplicon and Spectrum Instruments. In section II the necessary gas-sensing TDLAS-WMS details are introduced while section III gives a summary of the mechanical structure of the FLITES CST system. In section IV, a specification is presented, showing the need for custom design. In section V, we overview the design of the DAQ, pointing towards solutions that deliver the specifications. The results of characterization of the prototype DAQ is presented in section VI, while we conclude that full parallelism, high-speed and low-noise can be achieved by the DAQ nodes providing system readiness for gas concentration imaging.

II. TDLAS-WMS GAS SENSING: AN OVERVIEW:

To measure specified gas species concentration, this system uses tunable diode laser absorption with wavelength modulation spectroscopy (TDLAS-WMS) [2, 3, 9, 25], which has been previously applied to jet-engine research [26] and gas-sensing applications [27, 28]. By applying a current ramp (10-100 Hz sawtooth) to a narrow-wavelength laser, an optical beam is repeatedly wavelength-scanned across a previously measured absorption feature [2, 3, 29, 30]. For WMS, a secondary 10-500 kHz sinusoidal dither is applied [31] allowing phase sensitive detection [32] and digital lock-in amplification (DLIA) [19, 20, 21, 22]. The gas parameters [2, 3, 11, 29, 30, 33] and ultimately the path concentration integral (PCI) of the target gas along the beam [3, 7, 8, 25], can be inferred by using a spectroscopic curve-fitting model based upon the Beer-Lambert law and the known properties of the gas. This system targets CO_2 absorption [2, 3], which requires a 1997 nm seed laser. Due to the requirements for tomography – discussed below – the seed-laser is amplified using a 1.5-2.0-Watt Thulium-doped fiber amplifier (TDFA).

III. THE TOMOGRAPHIC SETUP: AN OVERVIEW:

To image the exhaust plume of commercial jet-engines, a 6-projection angle, 21-beam/projection (126-beam) array is formed using a custom 7 m diameter, dodecagonal mechanical ring structure [7]. This requires the light from the seed-laser and the TDFA to be distributed to transmit modules mounted on planar, parallel alignment plates [7, 8]. This approach reduces costs and allows simpler channel-channel synchronization by utilizing splitters with ratios 1:6 and 1:21, rather than 126 laser diodes of narrow and tunable line-width [29, 30]. The regular grid produced by this geometry allows a 1.8 m diameter central imaging space (~1.4-1.7 m exhaust plumes expected),

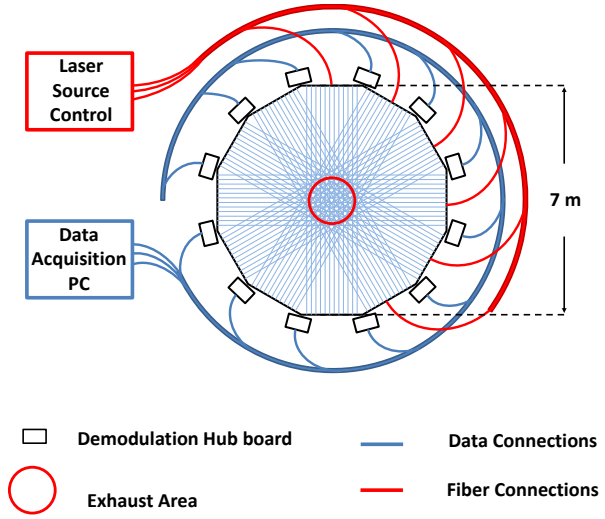

Fig.1. An overview of the imaging structure, adapted from [6], showing the central 126-beam array, dodecagonal mounting, the 1.4 m exhaust plume, the distribution (red) of 2 µm laser light using a TDFA and spliced fiber network, the 12-node DAQ and the back-end data network to the control PC (blue).

shown in Fig.1. To capture the TDLAS-WMS wavelength and amplitude modulated light after it has passed through the plume, receiver elements located on the alignment plates use extended InGaAs photodiodes with local, differential transimpedance amplification (TIA). This modular strategy, (where lasers, photodiodes and signal processing can each be easily replaced), gives the advantage of instrument scalability to other gas species. For example, for the current CO_2-specific wavelength, very few changes would be required to allow water vapor (H_2O) imaging. By carrying out the demodulation process of TDLAS-WMS upon the captured data, and by generating CO_2 PCIs for the many separate beam paths, the spatial distribution of gas concentration can be obtained by data inversion [9]. To date, this system has been proven by phantom tests replicating the expected

Fig.2. Detail (top) of an alignment plate showing mechanically supported fibers (yellow/black) to the transmit modules, and the preamplifier PCBs with ribbon cables (blue). Custom optical kinematic mounts, the 'ring' (red) during on-site build and fiber 1:21 splitter boxes are also shown (bottom). Visible in the center of the ring (bottom) is a propane gas-burner to provide deterministic placement and concentration CO_2 for phantom imaging tests.

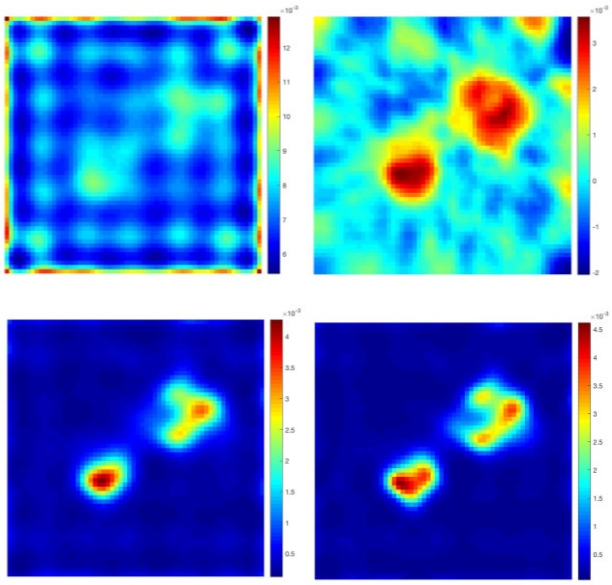

Fig.3. Experimental gas phantom reconstructions, replicating a dual phantom 60cm and 40cm tomographic imaging test from [8]. These compare a smoothing algorithm (A) with iterations 5, 10 and 15 of a positivity-constraining algorithm (B to D).

CO_2 concentrations and air temperatures [8], while tomographic methods have also been developed [10]. The detail of the mechanical structure, and the setup for imaging tests is shown in Fig.2, while experimental validation of gas concentration imaging and a preliminary investigation as to constrained algorithms are provided in Fig.3 [8, 10]. The reconstruction results show that, while under-determined due to costs, tomographic imaging can be performed with reconstruction artefacts of low-severity [10].

IV. Data Acquisition: Strategies and Specifications:

There are several application-level specifications necessitating a custom design in this context. The first is the ~70 m distance from photodiode preamplifiers to the test cell control room [12]. Naturally, noise pickup, cable costs and scalability for >256 beams requires a distributed DAQ architecture, similar to [13, 15, 16, 17]. To solve this, twelve or more digitization nodes can be hosted on the tomographic mounting ring [7]. As testing cells are industrial, high-vibration and high-contamination (oil, soot, water, fuel) environments [7], a pathway towards a rugged DAQ is needed. Likewise, equipment must not interfere with the jet-engine nor modify the aerodynamic properties of the cell. Distributing the DAQ allows reduction in system-level costs and at-site digitization affords advantages for digital signal processing (DSP) [19, 20] and data communications [11]. For the intended 126-beam imaging system, the 12 nodes yield a requirement of 10.5 channels/node. Forcing a binary value that is suitable for implementation i.e. 16 channels/node, allows redundancy or expansion along with PCB simplification through multi-ADC packaging. The presented 12-node DAQ therefore implements 192 channels.

The gas flow within the plume (100-200 m/s) necessitates a parallel design, although for suitable high sample-rate ADCs, low-ratio time multiplexing could be used to reduce costs. TDLAS-WMS supplies many of the specifications typical of DAQs, outlined in Fig.4. For low noise gas concentrations with minimal calibration, spectroscopists suggest the use of a first (1f) and second (2f) dual-harmonic normalization approach [3, 30, 33]. Assuming a 500 kHz maximum WMS sinusoidal dither (1f), the second harmonic will be at 1 MHz (Nyquist frequency of 2 MHz). However, this assumes only two points per period rendering a triangular wave rather than

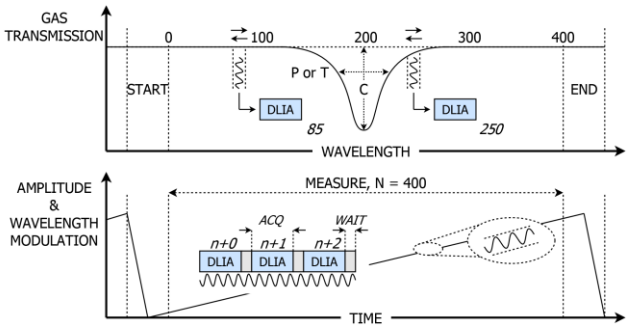

Fig.4. At the top, the gas absorption feature under interrogation, and at the bottom, the laser ramp and dither modulation, showing discrete DLIA calculation periods and the single dither-cycle waiting period between measurements.

a high purity sinusoid. As such, an oversampling factor of 10 to 20 is required giving a DAQ sample rate of 20-40 MS/s/channel. It has been suspected that the TDLAS wavelength ramp (10-100 Hz) also needs to be digitized, which suggests a frequency requirement of 6.3 Hz to capture the lower dv/dt of a 10 Hz sawtooth. AC-coupling allows the maximum input range and optimum bias-point of an ADC to be used without biasing shifts due to optical DC levels, however it has also been suggested that the DC component needs to be measured for characterization of the laser parameters [33]. While an AC-coupled range of 6.3 Hz to 2 MHz is specified, we note that lower noise-bandwidths could be achieved by an analog chain with -0.1 dB cut-off frequencies of i) DC to 63.6 Hz for a low-sample-rate path (suitable for a 100 Hz sawtooth dv/dt) and ii) 100 kHz to 2 MHz for a high-sample-rate path. The SNR is critical for tomographic reconstruction, where we aim for pixels giving absolute concentration measurement with an SNR of 30 dB. However, this is the noise of the final PCI after spectroscopic computation of gas concentration, 2f/1f-normalisation and the action of lock-in amplification. The SNR specification of the DAQ is therefore modest at 50 dB acknowledging that the gas plume itself is expected to be the dominant wide-band measurement noise contribution. The minimum effective number of bits of the ADC can be estimated from the 50 dB SNR requirement, where an 8-bit ideal ADC achieves 49.9 dB. A 2-bit design margin for non-ideal behavior can be used to establish the minimum ADC bit-width required, i.e. 10-bit. As the DLIA algorithm uses direct-digital-synthesis (DDS) of a reference signal, the spectral purity of this signal is also key. Matching the DDS bit-width to the 10-bit ADC, yields a minimum DDS spurious-free dynamic range (SFDR) of 60.2 dB. Of higher importance are i) a low gain non-uniformity between frequencies used for the 1f and 2f harmonic analysis, ii) low harmonic noise, i.e. >50 dB SFDR and iii) a linear gain response so that laser non-linearities within the spectroscopic models [2, 3, 29, 30] do not need to be augmented with electrical non-linearities.

Being a multi-channel node tasked with at-site digitization, signal processing and bi-directional communication, this custom DAQ must provide i) real-time DSP for in-phase (I) and quadrature (Q), first (1f) and second (2f) harmonic lock-in amplification (32-bit), ii) output of at least $N = 400$ discrete wavelength samples per ramp, iii) synchronization to the seed laser ramp and dither modulation frequencies, F_{ramp} and F_{dither}, iv) software control as to the lock-in frequency, f_{DLIA}, phase, ϕ_{DLIA}, time constant, τ_{DLIA} and experiment start, stop and reset commands and v) per-node output data rates between 58.6 Mb/s and 78.1 Mb/s [12]. A long-term design

Fig.5. A custom digitization node with a central FPGA (A), two octal ADC packages (B), main clocking phase locked-loop (PLL) (C), Ethernet communications (D) and initial analog filtering (E). Also included are i) SDRAM and FLASH memories, ii) PROM for FPGA configuration and bootloader, iii) a 3-axis accelerometer and iv) a 12-bit temperature sensor. Below the main PCB is a secondary power regulation PCB delivering ±5 V 1 A for up to 16 photodiode preamplifiers.

requirement of this system is that software control and in-the-field tuning of variables can be leveraged to allow adaptability of the instrument for different measurement methodologies [12, 33].

To aid sampling of the absorption feature, using the DLIA method, a per-DAQ-node state machine concept can be used with time periods equivalent to integer multiples of the dither period, $T_{dither} = 1/F_{dither}$. This allows short start, $(S = 100)$ and end, $(E = S + W)$ periods for laser settling and ramp fly-back, and $N = 400$ measurements made up of a maximum acquisition period, A_{max} and an inter-measurement waiting period, $W = 2$. The number of dither periods within a ramp, $T = F_{dither}/F_{ramp} = 5000$, can then be used with Eqn.2. to calculate the maximum acquisition, $A_{max} = 10$. The maximum DLIA time constant would then be $\tau_{DLIA} = A_{max}.T_{dither} = 200\ us$. While DAQs often use the precision-time-protocol (PTP) to allow highly accurate time synchronization of multiple units, in this case, the ramp and dither signals are buffered and distributed symmetrically to all DAQ nodes. This allows synchronization when using the per-DAQ-node state machine and allows synchronization with a laser driver that does not have PTP support.

$$T = S + N(A_{max} + W) - W + E \qquad \text{- Eqn.2.}$$

V. SYSTEM-LEVEL AND SUB-SYSTEM DESIGN:

This paper discusses the digitization node shown in Fig.5. [12]. This implements 16 fully-differential channels, each with a 1st order 10 Hz high-pass and a 2nd order 3 MHz low-pass response. When combined with the 3 MHz pole of the pre-amplifiers, a 3rd order anti-alias filter is formed. This is suitable for the 14-bit 10-40 MS/s ADCs when the frequency roll-off of the signal itself is considered. The octal ADC package (Analog Devices - AD9257) provides significant system-level cost savings above a bank of individual packages and in this case, this was sufficient to change from 10-bit to 14-bit. The clocking and data transfer strategy is shown in Fig.6, where each ADC provides low-voltage differential signals (LVDS) at 560 Mb/s to a central FPGA using a serializer-deserializer (SerDes) standard. The node therefore requires design for a raw data rate of 8.9 Gb/s, while the full 12-node system has a raw data rate of 107.5 Gb/s. This throughput is too large for real-time transmission and as such, requires the use of embedded real-time DSP that must decimate these data rates for available Ethernet

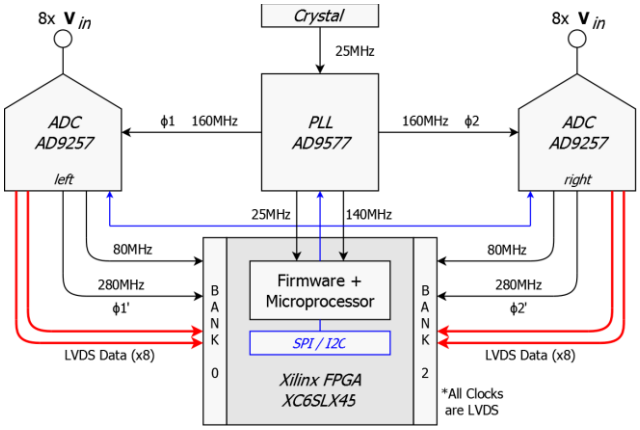

Fig.6. Clocking and ADC SerDes data architecture for a single digitization node. Each ADC provides 14-bit 10-40 MS/s data using source-synchronous low-voltage differential signaling (LVDS) to the central FPGA.

protocols (e.g. 100BASE-TX) [11]. The FPGA design for simultaneous acquisition and signal processing of multiple high-speed input channels is shown in Fig.7. The data, both raw from a selectable channel and processed via the DLIAs, is stored in two FIFOs before being passed to an embedded microprocessor. These FIFOs implement a 2-way wavelength-measurement interleaving process alleviating the effects of packet-loss observed within engine test cells [11]. The FPGA is used to implement the digital lock-in amplification method [19, 20, 21, 22]. This generates a local high-purity sinusoidal reference using DDS. The advantage of this is that within this measurement scenario, the reference can retain low-noise and suitable timing to the laser (Fig.4.), independent of the long cable distances. The lock-in method, shown in Fig.8. uses this reference as a multiplying homodyne oscillator to create the sum and difference frequency components. Choosing the difference using a low-pass filter, the input signal can be brought down to a DC magnitude and phase, with the ADC input data rate being decimated by the number of digital low-pass coefficients (taps). The number of unity-weighted coefficients within the DLIA low-pass accumulation filter, N_{taps}, for a sampling frequency, F_s (40 MS/s), a WMS dither frequency of F_{dither} (500 kHz), and an integer number of dither periods, A_{max}, within a measurement can be found from Eqn.3. While the number of required DLIA output bits, N_{DLIA}, can be established using Eqn.4, where N_{sig} is the bit-width of the ADC input signal (14-bit) and N_{ref} is the bit-width of the DDS reference signal (14-bit). For example, for both $N_{taps} = 160$ (for $A_{max} = 2$) and $N_{taps} = 800$ (for $A_{max} = 10$), a bit-width of 38 is suitable. The lower 6-bits can be truncated with minimal loss of precision.

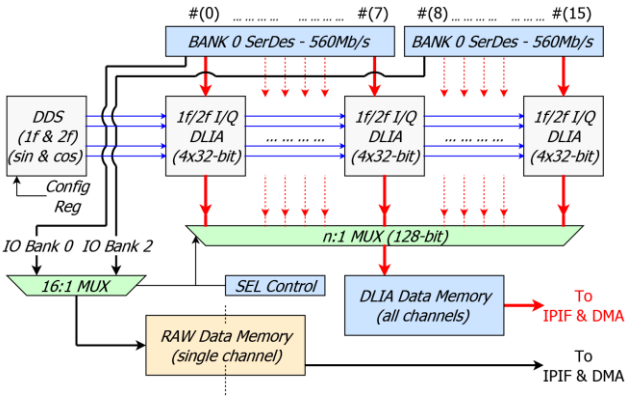

Fig.7. The ADC data capture, digital lock-in signal processing providing fundamental (1f) and 2nd harmonic (2f) in-phase (I) and quadrature (Q) 32-bit data. A secondary signal chain allows capture of full-rate raw ADC data.

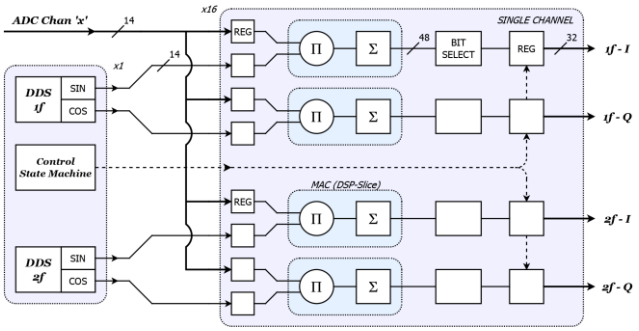

Fig.8. A single-channel digital lock-in amplifier (DLIA) shown with the shared direct-digital-synthesis (DDS) units. A shared controlling state machine allows a) synchronization with the laser and b) provides an accumulation sampling signal once the DLIA time constant is reached. The multiplication, Π and accumulation, Σ, are implemented using the multiply and accumulate (MAC) within the Xilinx DSP48A1 DSP slices.

$$N_{taps} = A_{max}\left({}^{F_s}/_{F_{dither}}\right) \qquad \text{- Eqn.3.}$$

$$N_{DLIA} = N_{sig} + N_{ref} + \lceil log_2(N_{taps}) \rceil \qquad \text{- Eqn.4.}$$

To provide software control and communications with a server within the control room, the backend of this design uses an embedded 32-bit RISC microprocessor [12]. The design of this is detailed in Fig.9. where the FIFOs within Fig.7. provide regular 'FIFO Full' flags which can be used as interrupts. When an interrupt is observed, the data is passed into working memory via direct-memory access (DMA), the data is then packaged into two data-frames and passed to the transmit buffer of the Ethernet medium-access-controller (EMAC). The receive buffer is periodically polled to allow waiting commands to be serviced. However, at present a basic task-sequential scheduling system is used.

VI. Data Acquisition: Characterization Results:

Each optical receiver uses an InGaAs photodiode directly-connected to a custom preamplifier and line driver to ensure good immunity to electrical interference from the test cell environment (Fig.10. inset). A differential structure is used with a transimpedance gain of 10.2 kΩ and a 3 MHz first-order low-pass. This ensures gain flatness for the dither and to start the frequency roll-off required for anti-alias filtering. While the presented DAQ is generic and can be used for other applications, the preamplifier design is driven by the optics and signal specifics of TDLAS-WMS. However, as the quantum efficiency tracks theory over a large wavelength range (900 nm-2100

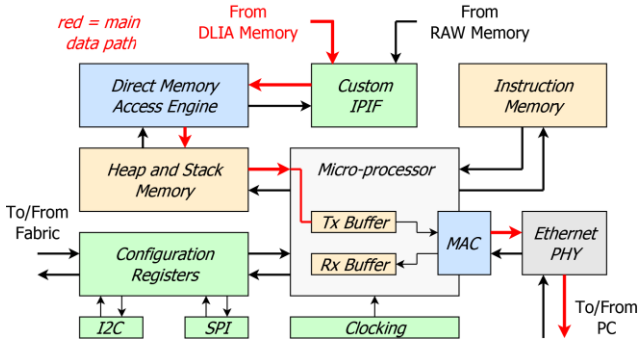

Fig.9. The structure of the back-end gate-level design. An intellectual property interface (IPIF) streams data from either a multi-channel DLIA FIFO or a single-channel raw data FIFO to the Micro-Blaze heap/stack memory using the DMA engine. Control registers are provided for fabric enables, resets, triggers and control parameters (DDS frequency/phase, DLIA filter taps etc.).

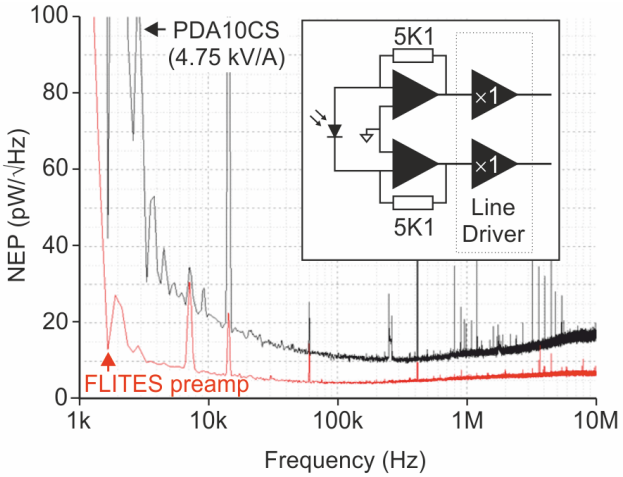

Fig.10. The noise equivalent power of the extended InGaAs photodiode pre-amplifier showing a comparison to the Thor Labs PDA10CS. Inset: A schematic of the differential 10.2 kΩ preamplifier.

nm), gas detection becomes a function of the laser wavelength and interrogation approach. This ensures this DAQ is applicable to a wide variety of chemical species. The intrinsic noise performance of the preamplifiers is similar to that of the popular Thorlabs PDA10CS (Fig.10.) but rejection of some, presumably common mode, interferers (e.g. those appearing at 13 kHz) is greatly enhanced. The differential line output interfaces directly to the differential signal path used in the digitization nodes. Fig. 3 shows that the photodiodes and custom pre-amplifiers function correctly, while a manufacturing 'signal-present' yield of 95% was achieved.

The analog front-end of the digitization node, (i.e. differential operational amplifier, high-pass and low-pass), frequency performance has been verified, where -3 dB cut off frequencies at 10 Hz and 3 MHz are observed. A pre-manufacture simulation showed an overall gain of -0.7 dB, while the measured 192-channel (12-node) median gain was -0.59 dB. A 100% operational yield (i.e. correct frequency response) and a gain spread of 1.3 dB (at 100 kHz) are exhibited. The capture of parallel multi-channel (16) analog signals at the data rates required (560 Mb/s), proved to be an area requiring significant complexity with respect to bit-capture and deserialization clocking and the correct framing of the 14-bit serial data. With correct high-speed data capture from the ADCs, Fig.11. shows the result of amplitude linearity testing of a single channel (node #7, channel #14) using pure 200 kHz sinusoids at 40 MS/s. As this is AC coupled, it acts to test all ADC codes within the 14-bit range and allows assessment as

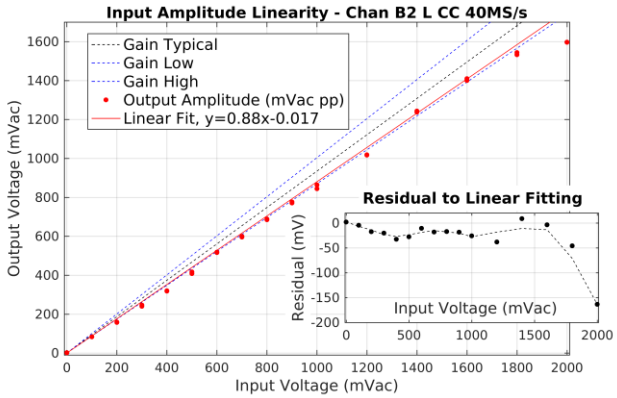

Fig.11. Input linearity with amplitude for a 200-kHz single-tone sinusoid at 40 MS/s. A linear fitting to the measured data shows agreement, in this case, to the minimum gain observed within the 192-channel tests. The residual between the data and the linear fit is presented inset

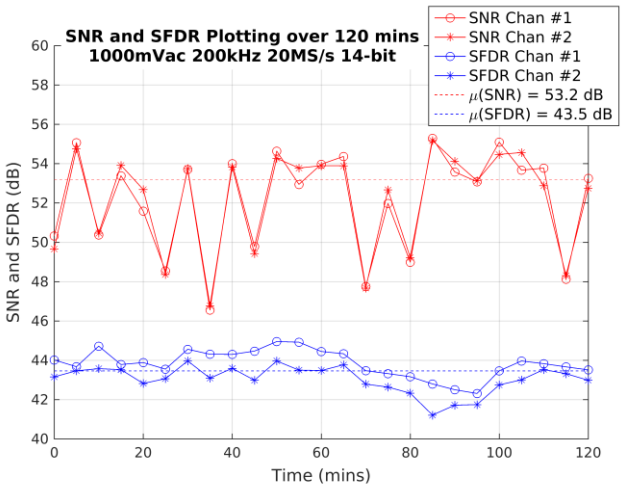

Fig.12. Long-term (2 hours) tests of the SNR (red), and SFDR (blue) for two channels of node #8. The input was a 1000 mVac-pp 200 kHz sinusoid. Each point is taken every 5 minutes and is formed of a 1000 sample acquisition at 20 MS/s.

to linearity issues within the analog chain. While the ADC has an input range of 2000 mVpp, Fig.11. shows a slight departure from linearity once the amplitude exceeds 1750 mVpp. Plotted alongside the measured data are lines representing the minimum, median and maximum gain terms from the gain uniformity statistics of all 192-channels. While linearity is important for the TDLAS-WMS spectroscopic modelling, the slight departures from linearity here will represent an error contribution far lower than that expected by the turbulence of the jet-engine plume. Here, non-linearity can be avoided by tuning the optical output power of the Thulium fiber amplifier. The DC offset, created after the input AC coupling, for node #7, channel #14 has also been measured at 3.0 mV. This can be removed using a per-channel long-term average, tested with the differential inputs shorted together. The resulting calibration value can be subtracted from the data prior to the DLIA.

With TDLAS-WMS being a lock-in frequency analysis method, the spectral purity and noise performance of an input frequency are crucial application-specific performance metrics for this DAQ. In Fig.12., both the SNR and the SFDR are plotted over the course of two hours for two channels in steps of 5 minutes. The reliability, in terms of ADC to FPGA data transfer frame locking and the overall noise from these channels is good, with the worst-case SNR and SFDR being 46.5 dB and 41.3 dB respectively, and best-case values being 55.4 dB and 44.8 dB

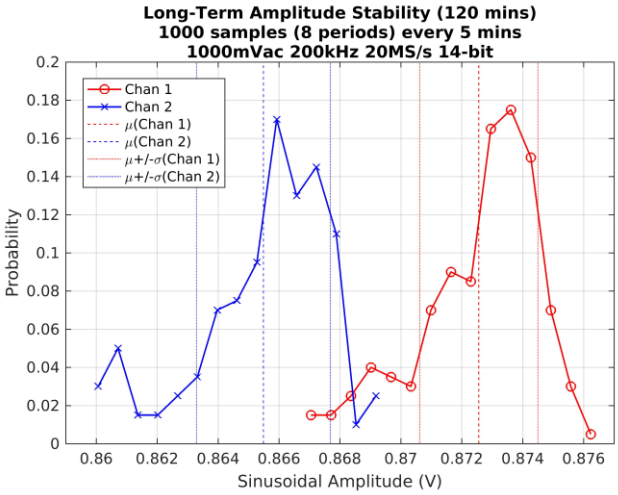

Fig.13. Amplitude stability over 120 minutes, observed using a 200 kHz 1000 mVac-pp sinusoid in 40 MS/s 14-bit mode. A measurement of 1000 samples per channel (approx. 10 periods, with 8 plotted) was repeated at 5-minute intervals. The mean amplitudes for two channels are 872 mV and 866 mV, with standard deviations of 1.9 mV and 2.2 mV, respectively.

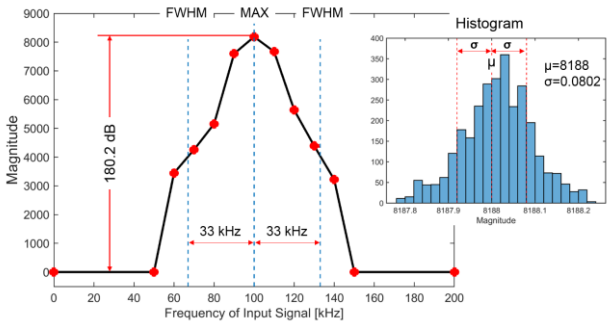

Fig.14. Frequency response of a 400-tap DLIA running at 20 MS/s using two DDS units for reference and a test sinusoid signal. Each point of in frequency domain is the mean of 500 DLIA samples with the two signals in phase. A FWHM of 66 kHz is obtained about the 100 kHz center. Long-term (5-min) histogram, inset, shows sub-LSB repeatability of the output data at the frequency maximum, albeit with a slight ($\Delta = 4$) deviation from the expected maximum.

respectively. However, a shorter-term test with data taken at 1-minute intervals showed maxima of 56.5 dB and 50.8 dB. We note that the prototype board itself includes digital switching noise from a variety of high-speed clock domains and does not yet have a specifically noise optimized analog signal chain. These noise figures are prior to the frequency selectivity, and hence noise reduction behavior of the DLIA. The average native (no input signal) noise floor of the system (node #14, channel #14) has also been measured at -60.4 dB for frequencies between 42 kHz and 20 MHz (at 40 MS/s). The histogram of this data shows that the noise is predominantly Gaussian but with a low (1.3%) probability of noise spikes of 3.5 mV. This noise floor agrees with the SNR measurements of pure-sinusoids, acknowledging that harmonic noise is also included in those measurements. In Fig.13. a histogram of amplitude stability for a pure 200 kHz 1000 mVac-pp sinusoid is presented for two independent channels over the course 120 minutes. This used a FIFO of 1000-samples to capture approximately 10 dither periods for which the amplitude was calculated per period. This was repeated at 5-minute intervals. While there is a slight offset between the channels ($\Delta V = 6\ mV$), possibly caused by gain variation of the analog circuits, both give low standard deviations of 1.9 mV and 2.2 mV respectively. The gain offset from the 1000 mVac-pp input is 0.59 dB and 0.62 dB replicating the earlier median pass-band gain.

For use within the DLIA algorithm, the TDLAS-WMS synchronization behavior of the DDS local sine and cosine references has been measured with respect to their controlling state machine state signal progression and the data readout chain. The two signals remain exactly 90 degrees out-of-phase ensuring orthogonal multiplication within the DLIA and as expected from the analytic expression: $SFDR_{DDS} = N_{ref} * 6.02 = 84.28\ dB$, the DDSs produce references with 83 dB SFDR.

While the temporal behavior of the DLIA has previously been tested with input TDLAS-WMS signals [19] and the frequency behavior of the DLIA algorithm is well defined [20, 21, 22], Fig.14. shows characterization of the 14-bit DLIA frequency response. This confirms a symmetric band-pass response with a full-width half-maximum (FWHM) of 66 kHz and a high rejection of out-of-band signals (180 dB). The magnitude standard deviation of $\sigma = 0.0802$, shows repeatability of the measurements over a 5-minute period. This complements bit-level verification of signal and reference multiplication and addition for a known period. There is a slight deviation from the expected maximum of 8192, however this may be due to a small phase angle, ($\phi = 1.8°$), between the reference and test signals (both DDS generated).

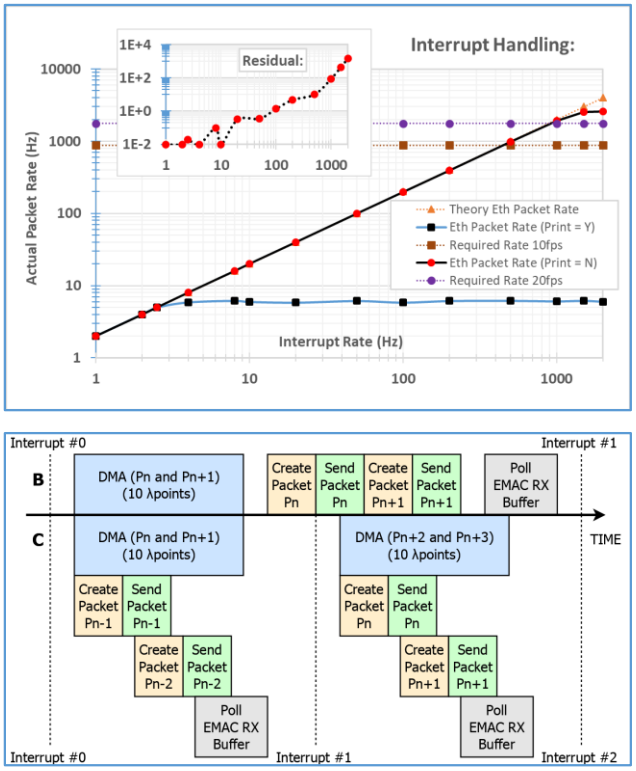

Fig.15. Interrupt handling for 88 Ethernet packets per TDLAS ramp (assuming all channels). The roll-off above 1000 interrupts/s includes an increasing probability of packets not being transmitted before the next interrupt, i.e. interrupt #2 supersedes and cancels interrupt #1. The packet rate reduces when on-board diagnostic facilities, are enabled (Print = Y).

As this DAQ node is intended for tomographic imaging, the rate at which it can acquire and process the data is crucial. For this purpose, when the FIFO is full (Fig.7) it interrupts the microprocessor to trigger a DMA transaction, Ethernet packet creation and transmission. Fig.15.A shows a plot of the interrupt rate vs the output rate of packets. This saturates at 2000 packets/second, which, assuming 88 packets per ramp per node, is suitable for 22.7 fps imaging ($N = 400$, 16 channels and 5 wavelength points per packet). At present, this process is implemented in a sequential manner (Fig.15.B), however DMA is intended to be operated in parallel, while the data buffers within the microprocessor working memory and the separate EMAC transmit buffer can be configured as a task-parallel pipeline (Fig.15.C). When combined with an increase in microprocessor clock frequency from 100 to 150 MHz, the limiting task will become the filling of the FIFO by DLIA data and a tomographic rate of 100 fps becomes achievable. Scalability to higher frame rates would be achievable with higher-specification microprocessors and a migration to standard 1Gb/s Ethernet networking.

VII. Discussion, Conclusions and Future Work:

A custom data acquisition system is presented for the quantification of jet-engine exhaust plume species. While there are several previous tomographic systems, such as Ma et al and Harley et al, that strive towards the same aims, this design represents a significant increase in physical size for the quantification of exhaust plume gas species in the largest civil aviation aero-jet-engines, such as the Rolls-Royce XWB. The tomographic instrument also includes a number of complexities with respect to optical, electrical and signal processing system requirements. From a data acquisition view, there are three requirements that differentiate this system from the available commercial DAQs. These are i) the scalability from 128 to 256 channels, ii) the suitability for user

implemented parallel, custom signal-processing running in real-time at the native data rate, and finally iii) the use of a true parallel acquisition architecture rather than the time-multiplexed methods employed by other multi-channel DAQs. The results pertain to the analog and digital performance of one digitization node providing 16 fully-differential 10-to-40 MS/s parallel acquisition channels with a native SNR of 56.5 dB. The full 12-node system provides 192-channels, along with FPGA-based lock-in amplification and is scalable to larger numbers of channels and different pollutant gases. The analog performance has been assessed and shown to meet the discussed design specifications, however there are two dominant factors that will affect the imaging quality, SNR and measurement uncertainty within the final tomographic reconstructions. The principal noise term is expected to be the natural uncertainty inherent within the jet-engine exhaust plume (i.e. the time-varying gas concentration over a 7 m path). The principal imaging uncertainty – manifested as artifacts and multiple solutions to the inverse problem – stems from the underdetermined measurement geometry and low numbers of angular views. In this paper, the noise and uncertainty of the data acquisition hardware has been characterized. However, we note that a complete assessment of uncertainty throughout the complex signal chain of optical, electrical and digital filtering processes, compounded by spectrographic modelling and tomographic reconstruction processes is outside of the scope of this current publication. Future work, installing this DAQ within the jet-engine test cell is underway while the presented DAQ can be improved though a second-generation prototype. Leveraging the pipelining of the digital-logic, direct-memory access and software can be used to increase the maximum tomographic imaging rate.

VIII. Acknowledgements:

The authors thank collaborators: Mr. B. Duncan and Dr T. Ouypornkochagorn (former Edinburgh), along with Dr D. McCormick (former Manchester). We are indebted to Dr V. Archilla (INTA) and Dr M. Johnson (Rolls-Royce) along with The University of Southampton and Royal Dutch Shell PLC.

IX. References:

1. Air Transport Action Group (ATAG), “Climate Action Takes Flight: The Aviation Sector’s Climate Action Framework”, White Paper, November 2015, Geneva Switzerland, URL: http://www.atag.org/component/downloads/downloads/311.html
2. J. Bain, M. Lengden, I. Armstrong, G. Stewart and W. Johnstone, “Development of Tunable Diode Laser Spectroscopy Instrumentation for Gas and Species Measurements in Harsh Environments,” Applied Industrial Optics: Spectroscopy, Imaging and Metrology, Arlington, Virginia, USA, 2013.
3. D. Wilson, I. Armstrong, M. Lengden and W. Johnstone, “In-situ Measurement of Combustion Produced CO_2 in the 2 μm Region, within a Jet Engine Exhaust Plume”, Proc. Field Laser Applications in Industry and Research (FLAIR), May 2014, Italy.
4. L. Ma, L. Xuesong, S. Sanders, A. Caswell, S. Roy, D. Plemmons and J. Gord, “50-kHz-rate 2D Imaging of Temperature and H_2O Concentration at the Exhaust Plane of a J85 Engine using Hyperspectral Tomography”, Optics Express, OSA, Vol 21, No 1, 2013
5. J. Harley, A. Rolling, C. Wisniewski and K. Gross, “Spatially Resolved Infrared Spectra of F109 Turbofan Exhaust”, Proc. SPIE Vol 8354, Thermosense: Thermal Infrared Applications, 2012

6. E. T. Turgut, M. Cavcar, O. D. Yay, M. Ucarsu, E. Yilmaz, O. Usanmaz, K. Armutlu and T. Dogeroglu, "A Gaseous Emissions Analysis of Commercial Aircraft Engines During Test-Cell Run", Atmospheric Environment, Vol. 116, p102-111, 2015.
7. P. Wright, D. McCormick, J. Kliment, K. Ozanyan, S-A. Tsekenis, E. Fisher, H. McCann, V. Archilla, A. Gonzalez-Nunez, M. Johnson, J. Black, M. Lengden, D. Wilson, W. Johnstone, Y. Feng and J. Nilsson, "Implementation of Non-Intrusive Jet Exhaust Species Distribution Measurements Within a Test Facility", Proc IEEE Aerospace Conference, Montana, USA, 5-12 March 2016
8. S-A. Tsekenis, N. Polydorides, E. Fisher, A. Chighine, J. Jia, H. McCann, D. Wilson, G. Humphries, M. Lengden, T. Benoy, W. Johnstone, J. Kliment, P. Wright, Y. Fend, J. Nilsson and V. Archilla, "Chemical Species Tomography of Carbon Dioxide", Proc. 8th World Congress on Industrial Process Tomography (WCIPT), Brazil, 2016
9. W. Cai and C. Kaminski, "Tomographic Absorption Spectroscopy for the Study of Gas Dynamics and Reactive Flows", Progress in Energy and Combustion Science, Vol 59, p1-31, 2017
10. N. Polydorides, S-A. Tsekenis, E. Fisher, A. Chighine, H. McCann, L. Dimiccoli, P. Wright, M. Lengden, T. Benoy, D. Wilson, G. Humphries and W. Johnstone, "A Constrained Solver for Optical Absorption Tomography", Applied Optics, Vol 57, 7, 2018
11. E. Fisher and T. Benoy, "Interleaving and Error Concealment to Mitigate the Impact of Packet Loss in Resource-Constrained TDLAS/WMS Data Acquisition", IEEE Trans. Instrumentation and Measurement (TIM), Vol 67, No 2, 2018
12. E. Fisher, S-A. Tsekenis, Y. Yang, A. Chighine, N. Polydorides, H. McCann, P. Wright, K. Ozanyan, D. Wilson, M. Lengden and W. Johnstone, "An Embedded Processing Design for 192-Channel 10-40 MS/s Aero-Engine Optical Tomography", Proc. IEEE International Instrumentation and Measurement Technology Conference (I2MTC), May 2018, Houston Texas, USA
13. S. Garcia Castillo and K. Ozanyan, "Field-Programmable Data Acquisition and Processing Channel for Optical Tomography Systems", Review of Scientific Instruments, Vol. 76, No. 9, 095109, 2005
14. J. D. Martinez, J. M. Benlloch, J. Cerda, C. W. Lerche, N. Pavon and A. Sebastia, "High-speed data acquisition and digital signal Processing system for PET imaging techniques applied to mammography," in IEEE Trans. Nuclear Science, Vol. 51, No. 3, p407, 2004.
15. G. Hegyesi, J. Imrek, G. Kalinka, et al "Ethernet Based Distributed Data Acquisition System for a Small Animal PET", 14th IEEE Real-Time Conference, Stockholm, Sweden, 2005
16. B. Hjertaker, R. Maad, E. Schuster et al, "A Data Acquisition and Control System for High-Speed Gamma-Ray Tomography", IOP Measurement Science and Technology, Vol 19, No. 9, p1-9, 2008
17. B. Humbert, P. Bard, C. Fuchs and D. Brasse, "Gigabit High Speed TCP Data Transmission for Positron Emission Tomography", IEEE Nuclear Science Symposium, p597, Florida, USA, 2009
18. P. Wright, K. Ozanyan, S. Carey, and H. McCann, "Design of High-Performance Photodiode Receivers for Optical Tomography", IEEE J. Sensors, Vol. 5, No. 2. p281, 2005.
19. A. Chighine, E. Fisher, S-A. Tsekenis and H. McCann, "TDLAS using FPGA-based Lock-In Detection for Multi-Channel Chemical Species Tomography", IEEE Sensors Conference, North Korea, Nov. 2015
20. S. Lascos and D. Cassidy, "Multichannel Digital Phase Sensitive Detection using a Field Programmable Gate Array Development Platform", Review of Scientific Instruments, Vol 79, 074702, 2008

21. M. Ayat, M. Karami, S. Mirzakuchaki and A. Beheshit-Shirazi, “Design of Multiple Modulated Frequency Lock-In Amplifier for Tapping-Mode Atomic Force Microscopy Systems.” IEEE Trans. Instrumentation and Measurement (TIM), Vol 65, No 10, 2016
22. J. Vandenbussche, J. Peuteman, and P. Lee, “Development of a Low-Cost Accurate Phase Measurement System,” 1st International Conference on Information and Communication Technologies Innovations and Applications (ICTIA), Tunisia, 2014.
23. L. Xu, R. Xue, Y. Li, H. Zhang and Z. Cao, "FPGA-Based Real-Time Implementation of Temperature Measurement via Tunable Diode Laser Absorption Spectroscopy," *in* IEEE Sensors Journal, Vol. 18, No. 7, p2751, 2018.
24. P. Cao, K. Song, J. Yang and K. Zhang, “A Real-Time Data Transmission Method based on Linux for Physical Experimental Readout Systems”, 18th IEEE Real-Time Conference, California, USA, 2012
25. K. Duffin, A. McGettrick, W. Johnstone, G. Stewart and D. Moodie, "Tunable Diode-Laser Spectroscopy with Wavelength Modulation: A Calibration-Free Approach to the Recovery of Absolute Gas Absorption Line Shapes," in J. Lightwave Technology, Vol. 25, No. 10, 3114-3125, 2007.
26. A. Sappey, L. Sutherland, D. Owenby, P. VanHoudt, J. Hannam, Q. Zhoa, P. McCormick, B. Masterson, M. Estes, “Flight-Ready TDLAS Combustion Sensor for the HIFiRE 2 Hypersonic Research Program”, AECD-TR-10-T-6, Final Project Report, 2009
27. M. Hamilton, G. Ritchie, Y. Arita, P. Ewart, “Multi-mode Absorption Spectroscopy, MUMAS, using Wavelength Modulation and Cavity Enhancement Techniques”, Applied Physics B, vol. 100, no. 3, p665-673, 2010.
28. A. Klein, O. Witzel, V. Ebert, “Rapid Time-Division Multiplexed, Direct Absorption- and Wavelength Modulation-Spectroscopy”, MDPI Sensors, Vol. 14, No. 11, 21497–21513, 2014
29. M. Bolshov, Y. Kuritsyn, and Y. Romanovskii, “Tunable Diode Laser Spectroscopy as a Technique for Combustion Diagnostics”, Spectrochimica Acta Part B: Atomic Spectroscopy, Vol 106, p45-66, 2015
30. G. Rieker, J. Jeffries, and R. Hanson, “Calibration-Free Wavelength Modulation Spectroscopy for Measurement of Gas Temperature and Concentration in Harsh Environments”, Applied Optics, Vol 48, 29, 2009
31. C. Goldenstein et al, “Infrared Laser-Absorption Sensing for Combustion Gases”, Progress in Energy and Combustion Science, Vol 60, p 132-176, 2017
32. T. Fernholz, H. Teichert and V. Ebert, “Digital Phase-Sensitive Detection for in situ Diode-Laser Spectroscopy under Rapidly Changing Transmission Conditions”, Applied Physics B Lasers and Optics, Vol. 75, No 2-3, p229, 2002
33. T. Benoy, M. Lengden, G. Stewart and W. Johnstone, “Recovery of Absorption Line Shapes with Correction for the Wavelength Modulation Characteristics of DFB Lasers”, J. IEEE Photonics, Vol 8, No, 3, 2016